Exploring in Electrochemical Behaviors and Anions Storage Characteristics of Carbonaceous Materials in Molten Salts Ni/$NiCl_2$-Graphite Battery

Wenlong Zhang[a], Huanxin Li[b,], Han Zhou[a] and Xiaohui Ning[a,]**

[a] Center for Alloy Innovation and Design (CAID), State Key Laboratory for Mechanical Behavior of Materials, Xi'an Jiaotong University, Xi'an, Shaanxi 710049, P. R. China

E-mail: xiaohuining@mail.xjtu.edu.cn

[b] Department of Chemistry, Physical & Theoretical Chemistry Laboratory, University of Oxford, South Parks Road, Oxford OX1 3QZ, United Kingdom

Email: huanxin.li@chem.ox.ac.uk

Abstract

Carbonaceous materials that possess reversible anions storage capacity and can worked as the cathode for Ni/$NiCl_2$-Graphite battery. However, differences in storage capacity of carbonaceous cathodes and factors affecting anions storage capacity have not been thoroughly investigated. Here, we systematically evaluated the electrochemical properties and intercalation reaction mechanism of carbonaceous materials cathodes firstly. Expanded graphite and graphite paper cathodes display the highest specific capacity of 72 mAh/g and diffusion-controlled capacity ratios (~98%). X-ray powder diffraction and Raman spectroscopy analysis on the graphite intermetallic compounds confirmed the presence of stage-5 intercalation/de-intercalation reactions. Density functional theory calculation and ionic diffusion model

analysis showed that the intercalation and diffusion process of $AlCl_4^-$ in graphite interlayers play a crucial role in anions storage reaction. Rich-in-edged outer graphite-layers are more conducive to form intercalation reaction active sites and store anions effectively. The expanded graphite electrode exhibits the highest intercalation reaction ratio ($\varphi_{R\text{-}GP}$ =1.40), confirming sufficient intercalation reaction active sites in each unit mass. And the multiple wrinkles and curled graphite sheets in expanded graphite provide adequate ionic transport/diffusion channels during electrochemical intercalation/de-intercalation reactions. Our findings provide significant support for understanding anions storage behaviors and designing cathodes with high anions storage capacity in the Ni/$NiCl_2$-Graphite battery.

Keywords

Ni/$NiCl_2$-Graphite battery; Cathode; Carbonaceous materials

1. Introduction

Developing new electrochemical energy storage technologies with high safety, long cycling longevity, and low material cost is a significant undertaking to meet the requirements of utilizing intermittent renewable resources[1]. In recent years, there has been a growing interest in developing novel electrochemical energy storage alternatives with cost-effective and high security. Since the 1980s, researchers have conducted extensive studies on various cathodes (including Mn_2O_4 and V_2O_5) to determine their electrochemical properties by utilizing reversible Al/Al^{3+} anode in room temperature ionic liquids (RTILs) electrolyte[2, 3]. However, the electrochemical reversibility and cycling stability of these metal compounds electrode materials can’t achieve

satisfactory performances and need to be further improved. In 2015, Dai et al reported a graphitic foam cathode with excellent electrochemical reversibility. They demonstrated intercalation/de-intercalation reactions of $AlCl_4^-$ among the graphite interlayers in $AlCl_3$/[EMIm]Cl ionic liquid[4]. The 3D graphitic foam cathode achieved a stable cycling capacity of around 65 mAh/g without capacity decay at 4A/g after 7,500 cycles, demonstrating fast anions migration and reversible intercalation/de-intercalation reactions. In addition, the graphite electrode in the molten salt electrolyte has also been proved to delivered benign electrochemical reversibility and higher electrode specific capacity of 190 mAh/g at 0.1A/g[5].

Thereafter, novel battery systems were proposed based on the intercalation/de-intercalation reaction of anions ($AlCl_4^-$, $Al_2Cl_7^-$ etc.) in graphite interlayers. For instance, the anode of the dual-graphite aluminum-ion battery mainly undergoes Al deposition/stripping reactions, and the formation/decomposition process of Al_xC[6, 7]. Due to the replacement of the metal aluminum anode with carbon materials, these new battery systems effectively alleviate potential risks, such as aluminum dendrites, surface passivation, and self-corrosion. In contrast, metal-graphite molten salt batteries with reversible conversion reactions of redox couples (such as Fe^{3+}/Fe and Ni^{2+}/Ni) in the anode rather than the deposition and stripping reactions of metal aluminum[8, 9]. These batteries not only possess high electrochemical activity in cathode materials and excellent ionic conductivity in molten chloroaluminate electrolyte systems, but they also differ from dual-carbon batteries. In the Ni/$NiCl_2$-graphite battery, electrode specific capacity of 350 mAh/g at 80 mA/g and energy density of 289 Wh/kg can be

obtained in the Ni/$NiCl_2$-C anode with inorganic molten salts ($AlCl_3$/LiCl/NaCl/KCl) used as electrolyte (working temperature of 95°C). Due to the low material costs and operating temperature, the Ni/$NiCl_2$-graphite battery is becoming an cost-effective and viable option for large-scale power storage devices in the future.

However, the Ni/$NiCl_2$-Graphite battery's performance is constrained by unclear reaction mechanisms and limited understanding of the intercalation/de-intercalation reactions in graphite cathode. Although the intercalation-type reactions have been observed in the graphite electrode paired with Al/Al^{3+} in molten salt electrolytes, it is possible that different electrochemical behaviors may occurred within specific potential ranges in the Ni/$NiCl_2$-Graphite battery. According to the Raman spectrum, Yu et al have demonstrated the existence of a stage 4-5 (average 4.2) intercalation reaction in the graphite cathode when paired with Al^{3+}/Al (0.5-2.2V) in $AlCl_3$/LiCl/KCl molten salt electrolyte[10]. While studies on graphite electrodes in molten salt electrolyte have indicated that there are few discernible changes in the G peak region during charging and discharging within the 0.5-2.15V range[11]. Additionally, graphene-based materials (such as defect-free few-layered graphene and 3D graphene foam) have demonstrated outstanding rate performance and stable cycling capacity when paired with Al^{3+}/Al, but the harsh processing conditions and the need for crystallite consistency are almost formidable tasks for massive production at a reasonable cost[12]. Therefore, investigating the electrochemical reaction mechanism between the graphite cathode and Ni/$NiCl_2$ electrode, as well as exploring the electrochemical properties of various carbonaceous electrode materials, holds significant potential for the

development of high-performance and cost-effective cathode materials for Ni/$NiCl_2$-Graphite molten salt battery.

Here, we comprehensively analyzed the electrochemical properties and structural characteristics of various commercial carbonaceous materials, including carbon paper, carbon felt, graphite paper, expanded graphite powder, and natural flake graphite powder, in both Ni/$NiCl_2$-Graphite batteries and Al^{3+}/Al half-cells. Non-graphitized carbon felt cathode exhibit the lowest electrode specific capacity of 2.3 mAh/g due to the lack of effective intercalated reaction sites. Among the graphitic cathodes, expanded graphite and graphite paper electrodes display the highest specific capacity of 72 mAh/g and diffusion-controlled capacity ratios (~98%), respectively. X-ray powder diffraction and Raman spectroscopy analysis on the intercalation reaction intermediate products of graphite paper cathode confirmed the presence of reversible stage-5 graphite intermetallic compounds during the charging/discharging. Subsequent density functional theory calculation and ionic diffusion model analysis showed that the intercalation and diffusion process of $AlCl_4^-$ in graphite interlayers plays a crucial role in the electrode storage capacity. Rich-in-edged outer graphite-layers architectures are more likely to form intercalation reaction active sites. The model evaluation based on the above results showed that the expanded graphite powder exhibits the highest intercalation reaction activity ratio ($\varphi_{R\text{-}GP}$ =1.40), confirming sufficient intercalation reaction active sites in each unit mass. And multiple wrinkles and curled graphite sheets provide adequate ionic transport/diffusion channels during the electrode intercalation/de-intercalation reactions.

2. Experimental

2.1 Reagents and materials

$AlCl_3$ (99%, Aladdin), LiCl (99%, Aladdin), NaCl (99.5%, Aladdin), and KCl (99.8%, Aladdin) were directly used in this work without any purification. Expanded graphite powder and natural flake graphite powder were purchased from Qingdao Huatai Graphite Co. Ltd (Qingdao, China). The Carbon paper (HCDO1N1), graphite paper and carbon felt were purchased from Suzhou Sinero Technology Co. Ltd and Six Carbon Technology Co., Ltd (Shenzhen, China). Foam nickel (thickness of 1.5 mm) was purchased from Shenzhen Guangshengjia New Materials Co., Ltd, and cleaned by ultrasonic in ethanol and 1M sulfuric acid before used. Metal aluminum (99.99%, 50μm) were purchased from Metal Materials Co., Ltd (Hefei, China).

2.2 Preparation of electrolyte

The electrolyte of the Ni/$NiCl_2$-Graphite battery and Al^{3+}/Al half-cell is quaternary molten salts ($AlCl_3$: LiCl: NaCl: KCl with molar ratio of 61:10:15:14), all salts were subjected to dehydration process at 120 °C using columnar resistance furnace which connected to glove box in Ar atmosphere. And then, the mixed salts were pre-melted at 200 °C for 48 h to ensure the molten salts mixed evenly. Simultaneously, high purity Al strips were added to remove impurities in the molten salts until the electrolyte become transparent. Finally, the pre-treated eutectic salts were grinded and collected. The above all operations also carried out in the glove box in Ar atmosphere.

2.3 Battery assembly and electrochemical tests

The chlorinated nickel foam electrode (named as the Ni/$NiCl_2$ electrode) worked

as the anode of Ni/$NiCl_2$-Graphite battery and the preparation process is similar to the previous literature[9]. The preparation of Ni/$NiCl_2$ anode are carried out by using the HCl chemical chlorination. The tailored Ni foam are ultrasonic cleaned in 1.0 mol/L H_2SO_4 for 5min, and then cleaned by ethanol and UP water. After drying at 60 ℃, Ni/$NiCl_2 \cdot xH_2O$ electrodes are obtained by chlorinated in flowing HCl/Ar atmosphere, in which the HCl mainly from the natural volatilization of concentrated HCl. Finally, Ni/$NiCl_2$ anodes are collected by removing crystal water at 400 ℃ for 6 h. The structure of the Ni/$NiCl_2$-Graphite battery is the same with the device that developed by our previous works. The assembly process of Ni/$NiCl_2$-Graphite battery mainly includes three steps: Firstly, to ensure sufficient wetting and contact interface between the electrolyte and electrodes during testing, the adequate pre-dissolution of the mixed solid electrolyte is executed in a quartz crucible at 150 ℃. Secondly, as shown in **Figure S1**, the molybdenum sheet, Ni/$NiCl_2$ electrode, and intermediate hollow sealing ring (PTFE components) are assembled in sequence, and then the dissolved electrolyte dropped into the sealing ring. Thirdly, cathodes and the molybdenum current collector are assembled after the added molten salt electrolyte cool down. The anode and cathode of the entire battery are finally conducted with copper plates, which are clamped with stainless steel fasteners and transferred to the air atmosphere for testing.

Different carbonaceous materials were tested as the cathode, in which expanded graphite powder (marked as EGP) and natural flake graphite powder (marked as NGP) were made by slurry-coating process. The mass ratio of active material, conductive carbon (Super P) and binder (5% Polyimide in Nitromethylpyrrolidone) was 80:10:10

(wt%). The current collector is metallic Mo sheets (99.9%) with thickness of 20 μm. In order to compare powder carbonaceous materials with the self-supporting materials, the average active mass loading is about 3.5-4 mg/cm^2. To exclude the influence of the anode on cell performance, the anode capacity of all tested cells remained in excess. The current density of the galvanostatic charge-discharge tests was 100 mA/g based on the cathode mass. As for the Al^{3+}/Al half-cell tests, high-purity Al sheets (S=0.79 cm^2) with thickness of 50 μm were used as the anode and reference electrode. Cyclic voltammetry with different scan rates were performed in the electrochemical window range of 1.4V-2.1V. Electrochemical impedance spectroscopy (EIS) was executed by using AUTOLAB(AT51792) in two electrodes, as applied perturbation sine wave with amplitude of 5mV and frequency range of 0.01-100000Hz. All circuits are simulated and analyzed using corresponding Nova 2.1 software.

2.4 Characterization of carbonaceous materials

The crystalline structures of carbonaceous materials were detected by the X-ray powder diffraction (XRD, X'Pert PRO, PANalytical B.V). The morphology of the cathode materials was analyzed by Scanning Electron Microscopy (SEM, Japan, SU6600). In order to evaluate the graphitization degree of different carbonaceous materials and confirm the reactions principle, the Raman spectra of the graphite paper electrode with different potentials were tested by the laser Raman Spectrometer (HORIBA). Raman spectra of all carbonaceous materials were obtained using a laser of 633 nm (1000 cm^{-1}-2000 cm^{-1}). Raman spectra of graphite paper with different voltage states were obtained using a laser of 532 nm (1000 cm^{-1}-3000 cm^{-1}).

Galvanostatic charge-discharge and cyclic voltammetry tests were completed by Neware battery tester (CT-4000-mA) and electrochemical workstation (CHI660e), respectively.

2.5 Calculation method and theoretical modeling

Computer modelling was used to understand the intercalation behaviors of $AlCl_4^-$ into different graphite layers. The Vienna Ab initio Simulation Package (VASP) was used for DFT calculation, with supplied projector augmented wave potentials for core electrons[13-15]. The generalized gradient approximation of Perdew-Becke-Ern-zerhof was used for the exchange correlation functional[14]. The conjugate gradient algorithm was used in the structural optimization of $AlCl_4^-$ in layer-1, layer-2, and layer-3 of graphite (The corresponding calculation models are shown in **Figure S6**), providing a convergence of 10^{-5} eV in total energy. The cut off energy was set to 500 eV with a 1×1×1 K-point mesh to represent the Brillouin zone. The intercalation behaviors of the $AlCl_4^-$ ion into layer-1, layer-2, and layer-3 of graphite were evaluated from the following equations:

$$\Delta E_{int}\ (AlCl_4^-\text{-in-layer1}) = E_{AlCl4\text{-in layer1}} - (E_{G\text{-layer1}} + E_{AlCl4^-}) \quad (1)$$

$$\Delta E_{int}\ (AlCl_4^-\text{-in-layer2}) = E_{AlCl4\text{-in layer2}} - (E_{G\text{-layer2}} + E_{AlCl4^-}) \quad (2)$$

$$\Delta E_{int}\ (AlCl_4^-\text{-in-layer3}) = E_{AlCl4\text{-in layer3}} - (E_{G\text{-layer3}} + E_{AlCl4^-}) \quad (3)$$

Where ΔE_{int} represent the energy barriers for $AlCl_4^-$ intercalate into the layer-1, layer-2, and layer-3 of graphite, while E is the free energy for different optimized structure models.

3. Results and discussion

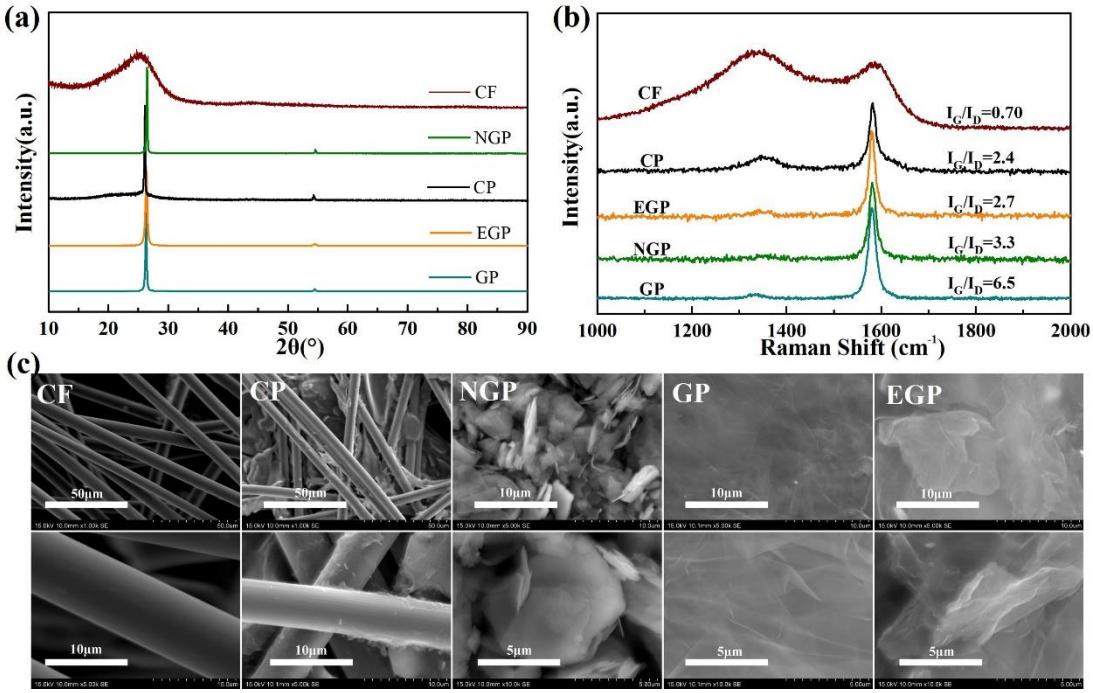

Figure 1 (a-b) XRD and Raman patterns of Expanded Graphite Powder (EGP Purple), Natural flake Graphite Powder (NGP green), Carbon Paper (CP black), Carbon Felt (CF orange) and Graphite Paper (GP blue). (c) SEM images of all as-selected electrode materials.

Based on the low melting point (~75°C) of the quaternary chloro-aluminic molten salt electrolyte, reversible solid-phase redox conversion(in 95°C) of metallic Ni and $NiCl_2$ has been proved in the anode of Ni/$NiCl_2$-Graphite battery[9]. However, the electrochemical performance of the graphite electrode is still limited by the low anion storage capacity and unclear intercalation/de-intercalation reaction mechanism. Firstly, to shed light on the relationship between carbonaceous materials characteristics and the electrode capacity, we systematically studied the electrochemical performances of commercial Carbon Paper (CP), Carbon Felt (CF), Graphite Paper (GP), Expanded Graphite Powder (EGP) and Natural flake Graphite Powder (NGP), in terms of energy

cost. We analyzed the crystallographic structure and graphitization degree of the different carbonaceous materials using XRD and Raman spectra, as shown in **Figure 1a-b**. Except for CF, obvious diffraction peak at 2θ=26° can be observed in the remaining four materials, manifests that few Graphite-2H crystal structure exists in CF. Indeed, the phase angle of the (002) plane diffraction peak corresponds to the interlayer spacing (d_{002}) in graphite. The diffraction peak position of the (002) plane in both NGP and EGP is closest to the ideal value of 26.4°, indicating that the interlayer spacing is about 3.35Å. In **Figure 1b**, the Raman spectra of all selected carbonaceous materials exhibit distinct peaks at ~1350 cm^{-1} and 1580 cm^{-1}, which corresponding to the vibration modes of defective carbon atoms and sp^2-hybridized carbon atoms, respectively. According to the intensity ratio (I_D/I_G) of these two peaks, the graphitization degree of carbonaceous materials can be well evaluated. As shown in **Figure 1b**, the I_D/I_G value (0.7) of CF is the smallest among all cathode materials, manifesting few graphite crystallographic structures existed in CF, which is consistent with the XRD results. Notably, apart from the highest I_D/I_G value (6.5) of GP, CP also has a comparable I_D/I_G value (2.4) to EGP (I_D/I_G =2.7), demonstrating that carbon fibers in CP possess highly ordered crystallographic structures. SEM was also used to explore the structural characteristics of all selected carbonaceous materials in **Figure 1c**. Both CF and CP are composed of simple carbon fibers with diameters of approximately 7.7 μm and 8.0 μm, respectively. According to the XRD and Raman results， the graphitization crystal structure in the CP electrode is much higher than that in the CF electrode, which may result in higher anions storage capacity during charging. EGP and

NGP both exhibit stacked blocks, but the main difference is that NGP showcases typical graphite flake stacking, while the surface of EGP exhibits multiple wrinkles and curled graphite sheets due to the exfoliation of the graphite blocks during expansion treatment. It is perceived that the expanded graphite structure contained in the EGP and GP electrodes provides high material utilization and electrolyte accessibility when paired with Al^{3+}/Al [16].

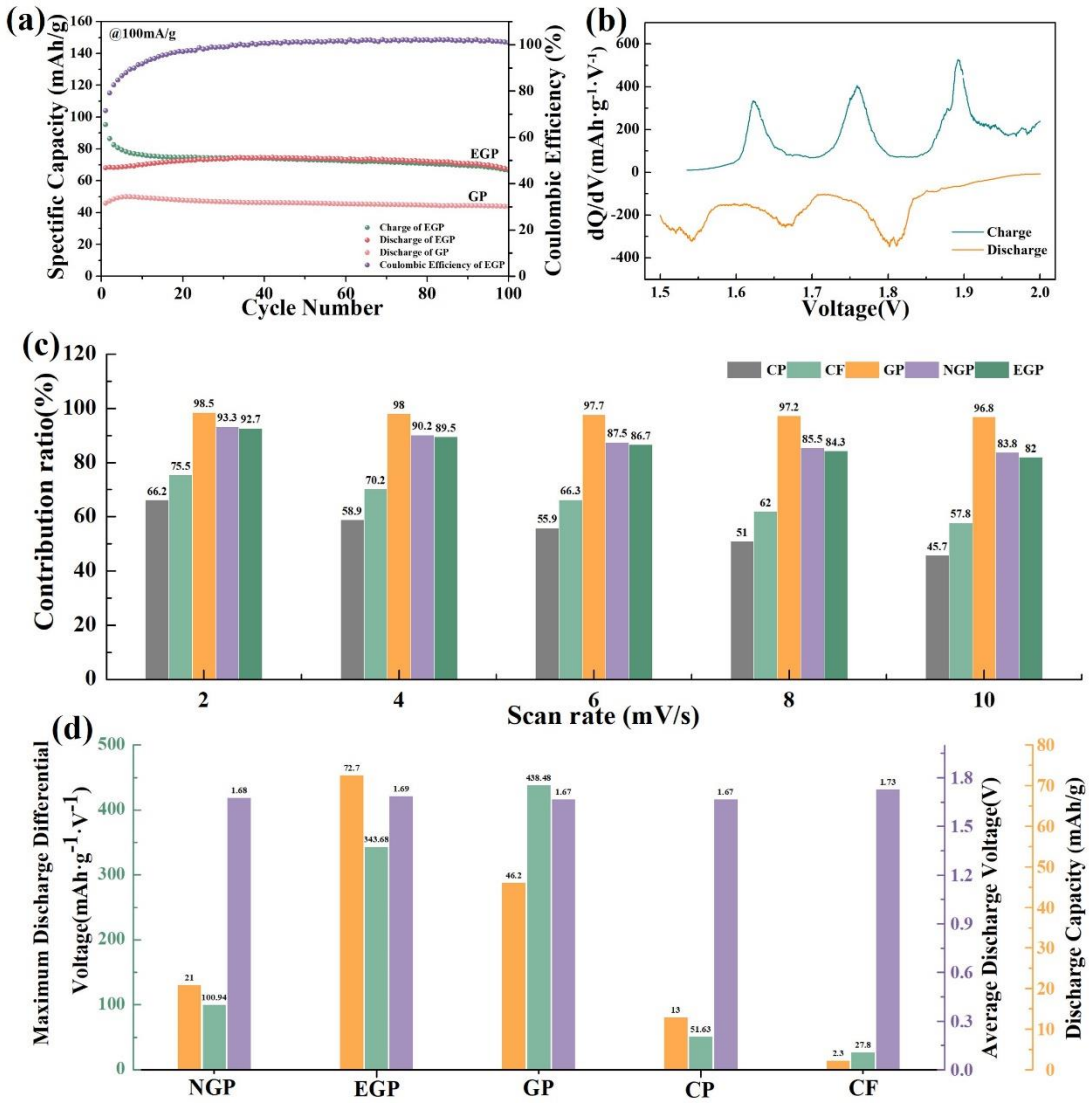

Figure 2 (a) Cyclic performances of GP and EGP electrodes; (b) Differential voltage curves of the EGP electrode; (c) Diffusion controlled capacity contribution ratios of all electrodes at various scan rates; (d) Electrochemical characteristics of the as-selected

electrode materials.

To accurately investigate the electrochemical performances of different electrode materials in Ni/$NiCl_2$-Graphite battery, excessive chlorinated nickel foam electrode (Ni/$NiCl_2$-NF) were used as the anode in all battery tests. Detailed cycling performances of CF, CP, NGP and GP electrodes at 100 mA/g were shown in **Figure S2-3,** CF and CP electrodes exhibit low electrode specific capacity of 2.3mAh/g and 13 mAh/g, respectively. Similar voltage platforms during the cycling in charge/discharge diagrams (in **Figures S3a-b**) suggest that the existence of stable electrode reactions in the electrode interface. However, the voltage curves of the CP electrode show more explicit charge-discharge plateaus than the CF electrode, which may be attributed to the higher graphitization degree of carbon fibers. These results confirm that carbon fibers with low graphitization degree are not ideal host materials for $AlCl_4^-$ intercalation, which is consistent with the case when paired with Al^{3+}/Al [17]. Among them, the EGP electrode (in **Figure 2a-b**) exhibited the best electrode specific capacity of 72.7 mAh/g, suggesting that highly expanded graphite and its derivatives may have greater potential in the development of high-performance cathodes for Ni/$NiCl_2$-Graphite battery. Distinct charge-discharge plateaus (in **Figures S3f**) at 1.62V/1.54V, 1.76V/1.66V and 1.89V/1.81V, which are mainly related to the intercalation and de-intercalation reactions of anions ($AlCl_4^-$, $Al_2Cl_7^-$etc.). Compared to the NGP electrode (20 mAh/g), high specific discharge capacity of 44 mAh/g in GP electrode suggests that expanded graphite possess obvious advantages in the electrochemical storage process of chloroaluminate anions over the graphite bulk. Among the graphitic electrodes, voltage

curves of EGP electrode display significant differences between the initial cycles and subsequent cycles, which are mainly because the insufficient electrode reaction in the initial few cycles. After the activation and stabilization process of anions diffusion during multiple intercalation/de-intercalation reactions, stable and reversible electrode storage capacity are obtained in the graphite electrodes, which is consistent with the capacity increase exhibited by graphite electrodes in molten salts AIBs[11]. According to previous researches about carbonaceous cathode materials in different battery systems in **Table S2**, high electrode specific capacity of carbonaceous materials can be obtained when versus aluminum anode in ionic liquid electrolyte at wide voltage windows. But carbonaceous cathodes based on surface adsorption storage mechanism can also exhibit comparable electrode specific capacity compared to graphite electrode materials. In the novel battery systems, such as initial anode free AIBs or dual ion batteries, the electrode specific capacity of graphitic cathodes are close to that of the EGP electrode in this work.

At the same time, electrochemical impedance spectroscopy (EIS) is also used to detect the interface reaction changes of cathodes before and after cycling, the interface impedance of different electrode processes can be effectively distinguished and evaluated by sine wave voltage ranging from low frequency to high frequency. The voltage frequency range applied on the open circuit potential is 0.01 to 100000 Hz, with an amplitude of 5mV. Corresponding test results are shown in **Figure S4**, the intercept between the curve in the high-frequency region and the real axis corresponds to the ohmic impedance or solution resistance (Rs) of the entire battery system. The two

semicircles in the medium frequency region reflect the two charge transfer impedances (Rct-01 and Rct-02) of the cathode, mainly including SEI film and faradaic process[16]. The inclined line in the low-frequency region represents the Warburg resistance (Wo), which corresponds to the diffusion process of anions in the electrode material[18]. In the low-frequency region, inconspicuous Warburg resistance in the CF and CP electrodes (in **Figure S4a-b**) before cycling are mainly attributed to the low electrode contactable area and poor bulk diffusion of carbon fibres. Graphitic electrodes (in **Figure S4c-e**) exhibit two electrode processes in the medium frequency region, which mainly involves the formation of SEI (Rct-01) and intercalation/de-intercalation reaction process (Rct-02). Corresponding electrode process parameters of all electrodes were quantified and compared in **Table S1** by simulation analysis of equivalent circuits (in **Figure S4f**). Resistances of all electrodes after cycling are significantly lower than before cycling, which mainly because the fully activating and wetting of the electrode interface during cycling[11]. The disappearance of Rct-02 in the CF electrode after cycling is mainly due to the low graphitization degree and intercalation/de-intercalation activity. In contrast, the Rct-02 of the CP electrode after cycling is 15.4 Ω, which is related to the higher degree of graphitization and storage capacity than that in CF electrode. As the expansion and contraction of graphite interlayers caused by intercalation/de-intercalation reactions, more interfaces and diffusion paths will participate in the electrode reaction, which leads to more significant impedance reduction in graphitic electrodes. Among them, the GP and EGP electrodes display low transfer resistances of 51.4 Ω and 47.1 Ω, indicating faster kinetics in electrochemical

reactions and anions diffusion rates than that in the NGP electrode.

To explore the differences in electrochemical energy storage of these electrode materials, cyclic voltammetry tests were performed at different scan rates (2-10 mV/s) and the corresponding results are shown in **Figure S5**. Excessive Al/Al^{3+} electrodes were applied as reference and counter electrodes to eliminate interference with the working electrode. The CV curves of the CF electrode exhibit completely different electrochemical reactions from those in other electrodes, mainly due to the low graphitization degree and graphitic proportion in carbon fibers. The CV test results for the EGP electrode in **Figure S5a** reveal broad oxidation peaks at about 1.80-2.0 V and reduction peaks at about 1.55-1.8 V, which correspond to intercalation reactions and the decomposition of GICs processes, consistent with results found in molten salt AIBs [10]. The CV curves of CP, NGP, GP electrodes also exhibit similar electrochemical behaviors with those of the EGP electrode at reduction (peak 2 and peak 3) and oxidation potential (peak 1), demonstrating that the electrochemical intercalation reaction of $AlCl_4^-$ is related to the degree of graphitization in electrode material. In general, electrode capacity includes the electrochemical reaction capacity and pseudo-capacitance at electrode interface. To evaluate the capacity ratio of different electrode materials, we calculated the b values for each according to the **Equation 4**. Typically, b values close to 1 indicate the capacitive process dominates electrochemical process, while those close to 0.5 suggest that the ionic diffusion-controlled process[5].

$$i = av^b \qquad (4)$$

To determine the capacity ratio of different electrode materials more accurately,

we calculated the average b value (denoted as $\bar{b}$), based on three distinct redox peaks in the CV curves of each material. The method used to calculate $\bar{b}$ is shown in **Figure S5b**. Excellent linear relationships existed in log(v) and log(i), $\bar{b}$ values of all electrodes were calculated using the above method, and the results are shown inside the corresponding figures. The $\bar{b}$ values of the GP and EGP electrode were closest to 0.5, indicating that the intercalation reaction of chloroaluminate anions ($AlCl_4^-$, $Al_2Cl_7^-$ etc.) in graphite interlayers dominated the electrode capacity storage. The $\bar{b}$ value of the CP electrode was closest to 1, manifesting that the capacity contributed by the capacitive reaction was the mainly way in capacity storage. However, it was difficult to determine the capacity contribution proportion of the NGP and CF electrode according to the $\bar{b}$ value. Therefore, we calculated the contribution ratio of the capacitive process and the diffusion-controlled process at different scan rates in all electrodes according to **Equation 5**.

$$i(V) = k_1 v + k_2 v^{1/2} \qquad (5)$$

Figure 2c shows that all electrodes based on graphite (GP, NGP, and EGP) exhibit high diffusion-controlled capacity with values of 98.5%, 93.3%, and 92.7% at 2mV/s, which indicates that the ionic intercalation/de-intercalation process is mainly electrochemical reaction during charging/discharging. In particular, the GP electrode exhibits an average diffusion-controlled capacity ratio of 98% at different scanning rates, suggesting the formation and decomposition of GICs in GP electrode are easily detectable and analyzable. On one hand, the test temperature (95 ℃) and potential range (1.4-2.1V) used in this study may affect the adsorption process of anions on the

electrode interface, resulting in low proportion of capacitive process. Previous research on expanded graphite electrodes in AIBs has shown that the proportion of pseudocapacitive contribution gradually decreases with increasing working temperature (from 35.6% at 20°C to 14.9% at 60°C)[16]. Furthermore, recent studies have shown that the capacitance contribution in the low potential range(0.5-1.4 V) is mainly due to adsorption behavior, while the capacitance contribution in the high potential range (1.5-2.4V) is mainly from reversible intercalation/deintercalation reactions[5]. On the other hand, the high ionic migration rate between graphite interlayers may contribute to the intercalation/de-intercalation reaction. The relevant theoretical calculation when versus Al^{3+}/Al implied that the large ionic migration rate or low migration energy barrier of $AlCl_4^-$ in intercalation processes may be beneficial for excellent rate performance[19]. It is worth noting that the contribution ratios of carbon fibrous (CP and CF) electrodes are 66.2 % and 75.5 % at 2 mV/s, indicating that the electrode capacity of carbon fiber contributed by the capacitive process cannot be ignored during electrode energy storage. The low capacity and high capacitive contribution ratio of CP and CF electrodes may be related to the high ion diffusion barrier inside the carbon fibers. The anions storage characteristics of this capacitive behavior have also been explored in previous studies (in **Table S2**), confirming that high electrode specific capacity can also be obtained under high surface area and wide cut off voltages in ionic liquid electrolyte AIBs.

To clearly compare the electrochemical characteristics of these electrode materials, electrochemical parameters of all electrode materials under the same test conditions are

summarized in **Figure 2d**. The average discharge voltages of these electrode materials were not significantly different, mainly due to the small voltage window (1.5-2.0V) in the Ni/$NiCl_2$-Graphite battery. But the differential voltage curves can reflect the electrochemical reaction potentials of different cathodes during the charging and discharging process. The maximum differential voltage of GP and EGP electrodes are 438 and 344 $mAh \cdot g^{-1} \cdot V^{-1}$, higher than other electrode materials, demonstrating higher intercalating reaction potential and superior in practical application. In terms of discharge specific capacity, the EGP electrode displayed the highest electrode specific capacity, implying higher material utilization rate and electrode energy density. The GP electrode has more advantages in practical applications for large-scale production due to the structural strength and without additional conductive and binding components[20, 21].

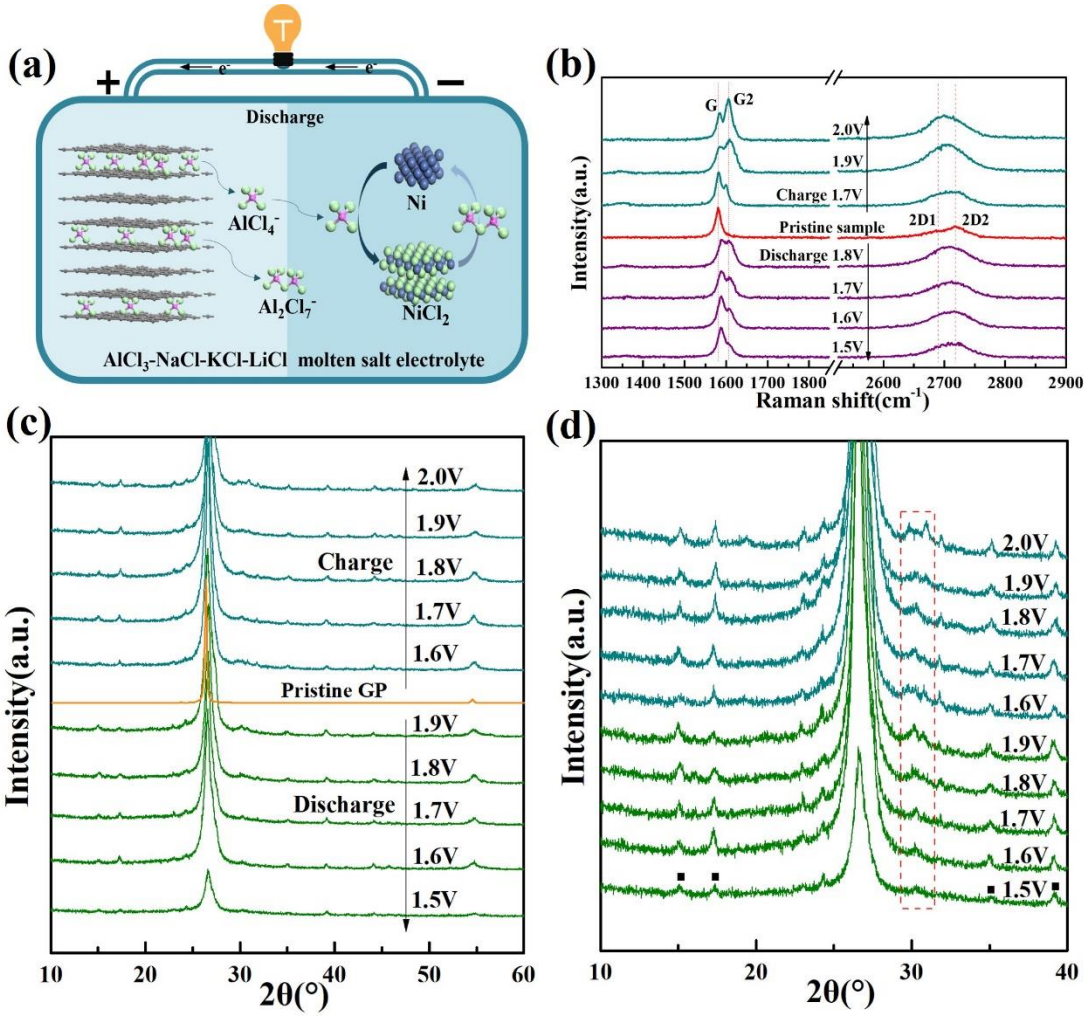

Figure 3 (a) Schematic diagram of the Ni/$NiCl_2$-Graphite battery; (b) Raman spectra of GP electrode at indicated cell potentials; (c-d) Ex situ XRD patterns at indicated cell potentials.

To clarify the reaction principles and structural change of the graphite electrode in the Ni/$NiCl_2$-Graphite battery (in **Figure 3a**). Considering the distinct intercalating reaction potentials and highest differential voltage peaks when versus the Ni/$NiCl_2$ anode. Binding-free graphite paper (GP) electrodes were used as cathode, and excessive chlorinated nickel foam electrode (Ni/$NiCl_2$) as anode to ensure that the GP cathode could fully participate in electrochemical reactions. To analyze the variation in vibration modes of carbon atoms in the GP electrode during intercalation/de-intercalation

reactions, we conducted ex-situ Raman spectra detection of GP electrodes at different cell voltages using a 532 nm laser with the laser power set at 3.2%. For comparison, we assembled pristine GP into the rest battery and subjected to the same conditions, except for the charging and discharging process. As shown in **Figure 3b**, the separate peak at about 1580 cm^{-1} corresponds to the E_{2g} phonon at the Brillouin zone center (also named as G peak), and the peak at about 1350 cm^{-1} is related to the breathing mode of six-atom carbon rings and associated with defects in graphite layers (named as D peak)[22-24]. Additionally, the peak at about 2710 cm^{-1} is attributed to the second order vibration mode of zone-boundary phonons. This peak in pristine graphite usually splits into two peaks with intensities of about 1/2 and 1/4 of the intensity of the G peak, which is also referred to as the G' peak in some literatures[25, 26]. For clarity, we named these two peaks at position about 2710 cm^{-1} as 2D1 and 2D2 peak, and marked at the corresponding positions in **Figure 3b**. Normally, the G peak is sensitive to electron transfer and re-orientation of graphite structure, which will split into derivative peaks and show wave-number shifts when GICs formed. These GICs are related to the type of intercalates and the structure of GICs such as $FeCl_3$, $AlCl_3$, and AsF_5 [27].

It can be observed that the position of the G peak becomes significantly up-shifts and splitting into a new G2 peak in 1602 cm^{-1} during charging, which mainly because of the different vibration modes in the graphene layers close to and away from the intercalation layers[28]. Therefore, we named these peaks at about 1575 cm^{-1} and 1601 cm^{-1} as E_{2g}(i) and E_{2g}(b), respectively, where E_{2g}(b) represents the vibrational mode adjacent to the intercalated graphene layers, and E_{2g}(i) is the graphene vibrational mode

away from the intercalated layers. According to **Figure 3b**, the split E_{2g}(b) peak gradually become distinct during charging process and weaken during discharging, confirming that electrochemical intercalation/de-intercalation reactions and the formation of GICs existed in the GP electrode [10]. Simultaneously, some reports have also shown that significant wave number differences between G and G2 appear when the stage index of intercalate reactions is larger than 3[27]. Referring to the subsequent analysis results of XRD, the stage index of the fully charged GP electrode is 5, which can be used to estimate the fluctuation of the reaction stage index during the entire charge-discharge process according to the following **Equation 6**:

$$R = \frac{I_i}{I_b} = \frac{\sigma_i}{\sigma_b}\frac{n-2}{2} \quad (n > 2) \tag{6}$$

Where R represents the relative intensity ratio (I_i/ I_b) of Raman doublet, σ_i and σ_b denote the Raman scattering cross sections of different graphene layers, respectively. The ratio(σi/σb) is a constant which is independent of the stage number n. But the ratio (σi/σb) is close to 1 in lithium-ion intercalation reaction, cannot be directly applied to the intercalation of $AlCl_4^-$. According to the XRD analysis of the fully charged GP electrode, the value of (σi/σb) is 0.63 after corrected by stage 5. The R values at different potentials are shown in **Figure 3b**, the GP electrode has the smallest R value(R=0.94) in the fully charged state, which corresponds to the smallest stage index(n=5). This suggests that the most adequate chloroaluminate anions intercalation behavior existed in the fully charged GP electrode. The estimation result of the stage index in all states demonstrates that the stage 5-6 intercalation/de-intercalation reactions mostly occurred during charging and discharging in the Ni/$NiCl_2$-Graphite

battery. Moreover, the change of 2D1 and 2D2 peaks can also be clearly observed during the charging and discharging process in this study. During charging, asymmetric 2D1 and 2D2 peaks in pristine GP gradually become symmetrical, the asymmetric disappearance of coupling peaks at about 2710 cm^{-1} derived from interlayer graphite carbon atoms is mainly because the vibration change of carbon atoms involved in intercalation reactions and the formation of graphite intermetallic compounds[25]. Similar phenomenon at 2D peak of graphite cathode in molten salt electrolyte has been detected in Yu's research work by using ex-situ Raman spectroscopy, the intercalation reaction of stage 4.6 in the fully charged cathode (2.15V) was calculated by the **Equation 6**([10]). This decoupled phenomenon has also been discovered in different intercalate compounds, Ferrarid et al observed the evolution of symmetry of 2D peak at about 2670 cm^{-1} by using Raman scattering and explored the intercalation reaction of anhydrous ferric chloride in few-layer graphite flakes[29]. It is inferred that there may be graphite intermetallic compounds of the stage 2 intercalation reaction based on the intercalation models about different graphene layers.

The results of ex-situ XRD tests on the GP electrode in different charge/discharge states when paired with the Ni/$NiCl_2$ anode are presented in **Figure 3c-d**. The XRD patterns of the GP electrode after electrochemical reactions and pristine GP both exhibit distinct diffraction peaks of (002) and (004) crystal planes at $2\theta=26.5°$ and 54.8°, suggesting that the layered structure of pristine GP are preserved after electrochemical reactions. However, there are several new diffraction peaks observed in the charged GP electrodes in the diffraction region ($2\theta<40°$), which are absent in the pristine GP. To

elucidate this, the fractions in 2θ=10°~ 40° was analyzed separately in **Figure 3d**. It can be observed that the intensity of diffraction peaks at 2θ=15.1°, 17.4°, 35.0 ° and 39.1° gradually increases during charging, indicating significant structural changes in the graphitic galleries due to the accumulation of intercalation products. these diffraction peaks are corresponding to the diffraction peaks of Al_2O_3(ICDD-04-016-7505), which mainly because the oxidation reaction of intercalation reaction compounds exposed to the air atmosphere when the sample transferred to the XRD equipment from Ar atmosphere[30]. These new diffraction peaks in the fully charged GP electrode are consistent with the XRD pattern of the fully charged (2.54 V) expanded graphite electrode when paired with Al^{3+}/Al anode in $AlCl_3$-ET electrolyte [31]. It was worth noting that two diffraction peaks at 2θ=29.8° and 30.9° (marked with a red rectangle) do not belong to $AlCl_3$ or Al_2O_3 or graphite analogues, and their intensity also increases with cell potentials, which is likely related to the formation and decomposition of graphite intermetallic compounds during the charging and discharging. It has been reported that when the molar ratio $AlCl_3$: XCl (X=Li, K, Na) of molten salts electrolyte is higher than 1: 1, more complex anions such as $Al_2Cl_7^-$ or $Al_3Cl_{10}^-$ may appeared except for the $AlCl_4^-$[11]. Since the molar ratio of the $AlCl_3$: XCl (X=Li, K, Na) electrolyte used in this study is 1.56:1, it is likely that anions other than $AlCl_4^-$ are also involved in the intercalation/deintercalation reactions. Therefore, the electrochemical reaction of the GP cathode can be expressed as the **Equation 7**, where n represents the number of graphitic carbon atoms involved in the intercalation reactions.

$$C_n + AlCl_4^- \rightleftharpoons C_n(AlCl_4) + e^- \qquad C_n + Al_2Cl_7^- \rightleftharpoons C_n(Al_2Cl_7) + e^- \qquad (7)$$

According to the in-situ XRD results by Dai et al in ionic liquid ($AlCl_3$: EMIC = 1.7:1.0) electrolyte, evolution laws and calculation of the stage number are further determined by theoretical model calculations based on different interlayer spacing[32]. It is observed that when the stage number of intercalation reaction in graphite is between 3-6, two diffraction peaks appear at 21-23° and near 27° respectively, due to the splitting of the peak at 26.5°. These peaks are referred to as $d_{(n+1)}$ and $d_{(n+2)}$, which corresponding to the inter-planar spacings. The splitting of diffraction peaks is also detected by using ex-situ XRD during the charging process in the molten salt electrolyte ($AlCl_3$/NaCl=1.8 in mol) by Jiao et al, new diffraction peaks appeared at 22.92°, 24.25°, and about 27° during the intercalation reaction by chloroaluminate anions into the graphitic carbon paper cathode[11]. According to the calculation of interlayer spacing, the inter-planar spacing ratios for the shoulder peak at 27.2° and separate peak at 23.1° are $d_{(n+1)}/d_{(n+2)}$ =1.18, which are consistent with the stage 5 intercalation reaction (the corresponding stage principles are shown in the **Figure S7**). Wang et al also conducted further analysis for the intercalation reaction in the pencil drawing graphite nanosheets cathode, two distinct diffraction peaks at 28.2°and 23.3°gradually formed as the charging process, stage 3 intercalation reaction was confirmed in the fully charged cathode by using the same calculation[33]. Comparing with the summary of storage mechanism in **Table S2**, high density intercalation reactions (stage 3 and state 4-5) in GP and pencil drawing graphite nanosheets electrodes when paired with Al anode, which may be attributed to the high charging cut off voltage of 2.35V and 2.2V.

Furthermore, it is observed that the new diffraction peaks (in **Figure 3d**) of the GP electrode, which emerge during charging, do not completely disappear during discharging. This is mainly because the trapped anions and the residual GICs that cannot be completely decomposed. It is important to note that lower reaction stage number corresponds to higher electrode material utilization and specific capacity. Therefore, stage 5 intercalation reactions in the GP cathode manifests exploring cathode materials with high specific energy is necessary to the Ni/$NiCl_2$-Graphite battery.

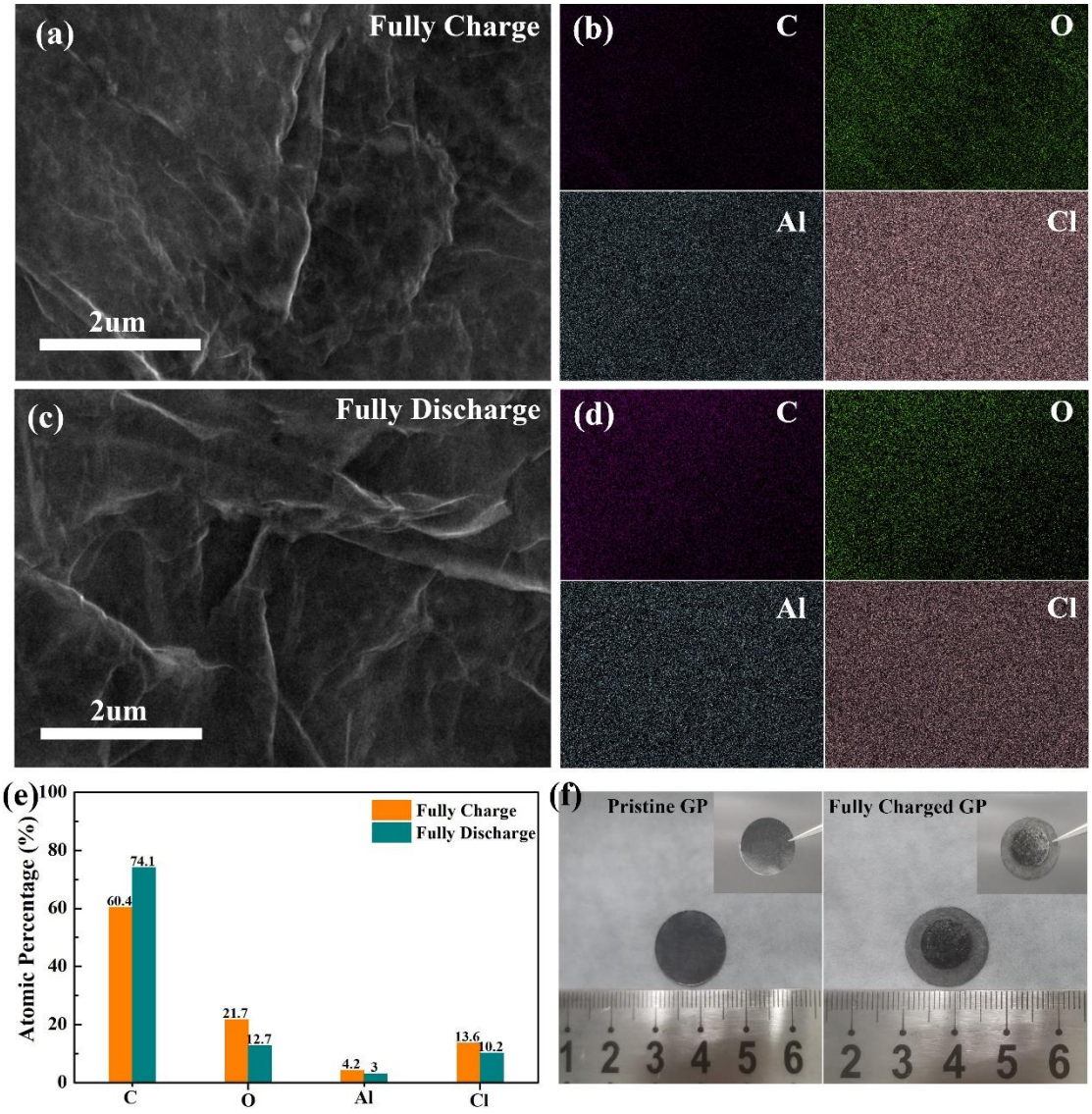

Figure 4 (a and b) SEM and EDS images of fully charged GP cathode; (c and d) fully

discharged GP; (e) The corresponding atomic percentage;(f) Optical pictures of pristine GP and fully charged GP.

Furthermore, the SEM and EDS images of the fully charged and fully discharged GP electrode were tested to analyze the morphology and element content changes in the material surface (as shown in **Figure 4a-e**). Compared with the pristine GP (in **Figure 1c**), on the surface of the fully charged GP electrode, many curved wrinkles can be clearly observed, while bumpy wrinkles are more prevalent in the fully discharged GP electrode. Additionally, optical images in **Figure 4f** show that the fully charged GP electrode exhibits obvious swelling after the desalination and drying process. These wrinkles on the surface of the GP electrode can be attributed to the expansion of graphene interlayers during anionic intercalation reactions. As evidenced by the expansion of graphite powder by about ten times after being charged when paired with Al^{3+}/Al in the molten salt (NaCl saturated $NaAlCl_4$ melt) electrolyte[34]. Therefore, wrinkles on the surface of GP electrode are mainly due to the expansion in graphene interlayers during anionic intercalate reactions. The variation in the graphene interlayer spacing during intercalation reactions has also been demonstrated in Al-Graphene batteries [35, 36]. The corresponding EDS mapping images show that the signals of Al and Cl elements are homogeneously distributed in the GP electrode after the charge and discharge process, verifying that the GICs mainly composed of Al, Cl and C elements during charging. The fully charged GP electrode exhibits higher surface content of Al (4.22%) and Cl (13.6%) elements, and lower content of C (60.44%) element, indicating that partial GICs undergo reversible decomposition process during discharging. The

remaining Al and Cl elements contained in the fully discharged GP cathode are mainly from the trapped $AlCl_4^-$ anions and insufficient decomposition, which is a common phenomenon in graphite cathode[5]. In addition, signal of O element may be due to the oxidation reaction of the active substances during washing and drying. These test results confirm that the existence of corresponding GICs during intercalation reactions, keep in line with experimental results in XRD and Raman.

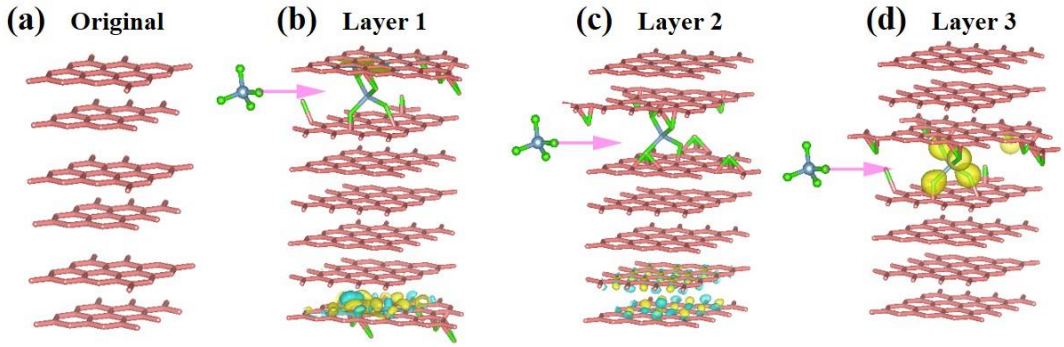

(e)

Calculation of binding energies(eV)			
$AlCl_4^-$ in Graphite surface			
$E_{AlCl_4^-}$(eV)	$E_{G-Layer1}$(eV)	$E_{AlCl_4^-\ in\ Layer1}$(eV)	$\Delta E_{bin(AlCl_4^-\ in\ Layer1)}$ (eV)
-15.99	-958.69	-969.59	5.09
$AlCl_4^-$ in Graphite layer-2			
$E_{AlCl_4^-}$(eV)	$E_{G-Layer2}$(eV)	$E_{AlCl_4^-\ in\ Layer2}$(eV)	$\Delta E_{bin(AlCl_4^-\ in\ Layer2)}$ (eV)
-15.99	-958.99	-967.58	7.40
$AlCl_4^-$ in Graphite layer-3			
$E_{AlCl_4^-}$(eV)	$E_{G-Layer3}$(eV)	$E_{AlCl_4^-\ in\ Layer3}$(eV)	$\Delta E_{bin(AlCl_4^-\ in\ Layer3)}$ (eV)
-15.99	-958.65	-965.58	9.05

(f)

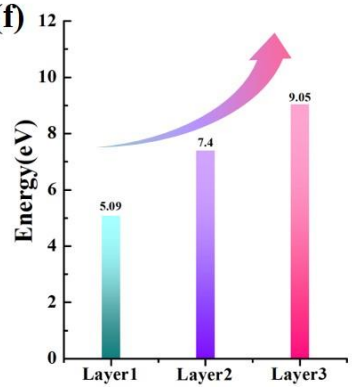

Figure 5 (a) Natural graphite structure model, intercalation of the $AlCl_4^-$ into different layers of graphite: (b) layer1, (c) layer2 and (d) layer3 (The cyan and yellow indicate electron depletion and accumulation, respectively. The pink present C atoms and bonds); (e) Energy profiles of different structural models; (f) Intercalation energy barriers of the $AlCl_4^-$ ion into different layers of graphite.

To understand the intercalation behaviors of anions into different graphite layers, we conducted density functional theory (DFT) calculations to reveal the redox

mechanism of $AlCl_4^-$ ions in different interlayers of graphite. The natural graphite model was shown in **Figure 5a**, where the layer spacing is approximately 0.34 nm. There three different graphite models with interlayers expanded to approximately 0.55 nm were illustrated, $AlCl_4^-$ ions intercalated models with optimized structures and differential charge density were demonstrated in **Figure 5b-d**, which revealed electron redistributions and strong interaction between $AlCl_4^-$ ions and graphite after the intercalation process. The detailed energy profiles for different models were listed in **Figure 5e**, where the ΔE_{bin} for all the layers are positive, revealing that the intercalation behaviors of the $AlCl_4^-$ ions require additional energies. **Figure 5f** indicated that the additional energy value increases for the intercalation from layer-1 (5.09 eV), layer-2 (7.40 eV) to layer-3 (9.05 eV), suggesting the intercalation of $AlCl_4^-$ ions into the outer layers is easier than that into the inner interlayers. In other words, the intercalation of chloroaluminate anions ($AlCl_4^-$, $Al_2Cl_7^-$ etc.) in inner interlayers of bulk graphite requires higher energy barriers than that in the outer graphite interlayers. Furthermore, our calculation results (shown in **Figure S8**) for the adsorption process of $AlCl_4^-$ on the graphite surface reveal that this adsorption process (ΔE_{bin}= -1.06 eV) is more spontaneous and exhibits lower energy barrier than the intercalation reaction. Therefore, it can be inferred that the adsorption process may existed at low electrode potential during the charging/discharging process, and the corresponding intercalation process may occur at high potential due to the different bonding strength.

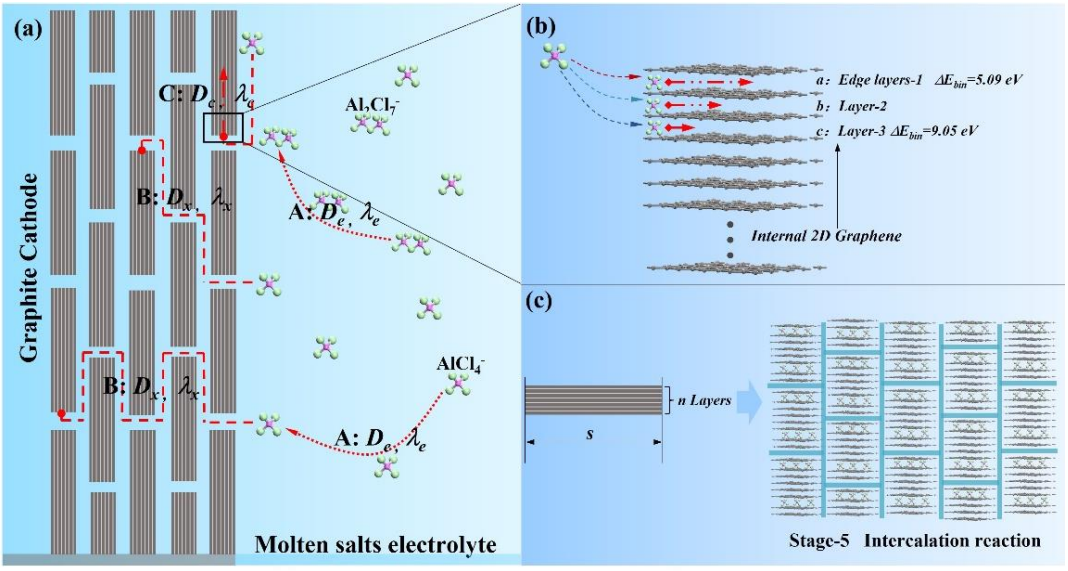

Figure 6 (a) Anions diffusion and transportation models in graphite cathode of Ni-Graphite battery structure model. (b) Intercalation reaction model of anion in edge layers graphite. (c) Analysis of reaction ratio(φ_R) based on stage-5 intercalation mechanism.

Table 1. Summary of physical and electrochemical properties of as-tested electrode materials

Samples	Mass loading (mg/cm²)	Unit characteristics	Thickness (μm)	Unit thickness (μm)	Intercalation Reaction ratio φ_R
CF	3.9	Carbon fibers	15	d~7.7	0.03
CP	4.2	Graphite fibers	15	d~8.0	0.16
NGP	~3.5	Graphite powder	20	0.2-1.0	0.41
GP	4.0	2D Graphite sheets	25	0.1-0.25	0.98
EGP	~3.5	3D Graphite sheets	20	0.02-0.1	1.40

Based on the above tests and calculation results in the cathode of Ni/$NiCl_2$-Graphite battery, we further improved a reaction model for the anionic diffusion and intercalation reaction in different cathode materials during the electrochemical reaction in **Figure 6**. Ionic diffusion in the electrochemical intercalation reaction mainly

includes the following three categories (in **Figure 6a**). (I) Ionic diffusion in the electrolyte, where the corresponding diffusion distance and diffusion coefficient are denoted as λ_e and D_e respectively. These parameters do not differ significantly among different cathodes due to the same molten salt electrolyte and assembly condition. (II) $AlCl_4^-$ ions migrate inside the cathode material, which display some differences in diffusion distance and diffusion coefficient (λ_x, D_x) due to the variation in surface structure and unit size among different cathode materials[18]. It is generally believed that electrodes (such as the GP electrode) with densely packed 2D graphite flakes structures may have longer diffusion distances and limited electrolyte accessibility interface than 3D porous architectures[37]. For example, EGP cathode with multiple wrinkles and curled graphite sheets has more advantages in providing electrolyte buffer spaces and improved ionic migration[38]. (III) The diffusion process of $AlCl_4^-$ ions within graphite interlayers, where the corresponding diffusion distance (λ_c) and diffusion coefficient (D_c) mainly depend on the internal structural characteristics of the graphite material, such as interlayer spacing, graphene layer numbers, defects condition etc. It is worth noting that $AlCl_4^-$ ions undergo intercalation reactions at the edge of graphite layers before diffusion in graphite interlayers, and the intercalation reaction sites directly affect the intercalation reaction concentration and electrode storage capacity. According to our DFT calculation results under the stage-5 reaction model (in **Figure 6b**), the energy barrier for $AlCl_4^-$ intercalation reaction with the outer graphite layer (layer-1=5.09 eV) is lower than that of the inner layer (layer-3=9.05 eV), and as the intercalation position approaches the graphite interior, the reaction energy barrier

gradually increases. Combining the CV test results, it can be inferred that these edged outer graphite-layers which can be contacted by the electrolyte, are the primary active sites for intercalation reactions and contribute to most of the storage capacity. In order to further quantify the difference in intercalation reaction active sites, we evaluated all tested cathode materials using a unified Intercalation Reaction Ratio (φ_R), as shown in **Equation 8**.

$$C = \varphi_R \frac{z \cdot \eta \cdot F}{M_{stage-5}} \quad (8)$$

Where z and η denoted as the number of transferred electrons and unit intercalation reaction number, $M_{stage-5}$ represents unit molar mass. Obviously, the larger the φ_R value, the closer of the saturation state of the stage-5 type intercalation reaction occurs within the unit structure. In order to limit the unified actual reaction capacity, ($\varphi_{R\text{-}GP}$) parameters of the GP electrode have been used as a unified reference standard. The calculation results are shown in **Table 1**, and EGP exhibits the highest intercalation reaction ratio of $\varphi_{R\text{-}GP}$ =1.40, indicating that the active sites for stage-5 intercalation reaction inside the material are 1.43 times higher than GP electrodes and 8.75 times higher than CP cathode which possess the similar graphitization degree. The results indicate that intercalation reaction active sites present in the EGP cathode are significantly higher than those in the CP electrode. As for the diffusion process of $AlCl_4^-$ ions in graphite interlayers, according to the DFT calculation results of $AlCl_4^-$ ions in few-layered graphene and graphite (D_c=2.2×10^{-9}cm^2/s^{-1}), the diffusion coefficient ($D_{c\text{-}6}$=3.3×10^{-9}cm^2/s^{-1}→ $D_{c\text{-}2}$=5.0×10^{-7}cm^2/s^{-1}) of in few-layered graphene only increases exponentially when the number of graphene layers is less than 6[18]. In most graphite

cathode materials tested, the number of graphene layers is much greater than this value.

According to the analysis of diffusion and intercalation reaction processes, it can be concluded that: (i) In graphite cathode materials of Ni/$NiCl_2$-Graphite battery, the ionic diffusion and transfer processes and the active sites of intercalation reactions determine the electrode storage capacity jointly. (ii) The multiple wrinkles and curled graphite sheets of EGP cathode provides richer ionic transfer and diffusion channels than densely stacked planar graphite flakes in GP electrode. Meanwhile, the lower unit structure thickness and rich-in-edged outer graphite-layers of EGP exhibit a higher intercalation reaction ratio ($\varphi_{R\text{-}GP}$ =1.40). (iii) The unit structure size (n, s) of electrode materials not only affects the ionic diffusion efficiency, but also impact on the intercalation reaction active sites significantly. Graphite materials with rich-in-edged outer graphite-layers can effectively improve the intercalation reaction ratio.

4. Conclusion

In this study, we analyzed the electrochemical behavior and structural characteristics of various commercially available carbonaceous materials, including carbon paper, carbon felt, graphite paper, expanded graphite powder, and natural flake graphite powder, in both Ni/$NiCl_2$-Graphite battery and Al^{3+}/Al half-cell. Our findings indicate that expanded graphite and graphite paper cathodes possess the most optimal anion storage capacity and intercalation reaction platforms at 1.8-1.9V. XRD and Raman analysis on the intercalation reaction intermediate products confirmed the presence of reversible stage 5 graphite intermetallic compounds during the charging/discharging process. With the assistant of DFT calculation and diffusion

model analysis, the intercalation and diffusion process of $AlCl_4^-$ in graphite interlayers plays a crucial role in the electrode storage capacity. Rich-in-edged outer graphite-layers architectures are more likely to form intercalation reaction active sites. Among all electrode materials, the EGP electrode exhibits the highest intercalation reaction activity ratio ($\varphi_{R\text{-}GP}$ =1.40), confirming sufficient intercalation reaction active sites in each unit mass. And the multiple wrinkles and curled graphite sheets of EGP cathode provides more ionic transport/diffusion channels than densely stacked planar graphite flakes in GP electrode.

CRediT authorship contribution statement

Wenlong Zhang: Writing–original draft, Data curation, Conceptualization, Methodology, Formal analysis, Investigation. Huanxin Li: Software, Resources, Methodology, Validation, Writing – review & editing. Han Zhou: Validation, Formal analysis, Visualization. Xiaohui Ning: Project administration, Conceptualization, Funding Acquisition, Writing – review & editing, Supervision.

Declaration of competing interest

All authors declared that they have no competing interests in this work.

Acknowledgments

This work was supported by grants from the National Natural Science Foundation of China (U1766216, 51874228) and Natural Science Foundation of Shaanxi Province (2020JM-068).

References

[1] S. Chu, A. Majumdar, Nature, 488 (2012) 294-303.

[2] M.P. Paranthaman, G. Brown, X.-G. Sun, J. Nanda, A. Manthiram, A. Manivannan, ECS Meeting Abstracts, MA2010-02 (2010) 314-314.

[3] N. Jayaprakash, S.K. Das, L.A. Archer, Chemical Communications, 47 (2011) 12610-12612.

[4] M.-C. Lin, M. Gong, B. Lu, Y. Wu, D.-Y. Wang, M. Guan, M. Angell, C. Chen, J. Yang, B.-J. Hwang, H. Dai, Nature, 520 (2015) 324-328.

[5] S. Guo, H. Yang, M. Liu, X. Feng, Y. Gao, Y. Bai, C. Wu, ACS Applied Materials & Interfaces, 13 (2021) 22549-22558.

[6] S. Wang, S. Jiao, W.-L. Song, H.-S. Chen, J. Tu, D. Tian, H. Jiao, C. Fu, D.-N. Fang, Energy Storage Materials, 12 (2018) 119-127.

[7] Z. Li, J. Liu, B. Niu, J. Li, F. Kang, Small, 14 (2018) 1800745.

[8] T. Dai, L. Yang, X. Ning, D. Zhang, R.L. Narayan, J. Li, Z. Shan, Energy Storage Materials, 25 (2020) 801-810.

[9] W. Zhang, C. Liao, X. Ning, Chemical Engineering Journal, 435 (2022) 135110.

[10] J. Wang, X. Zhang, W. Chu, S. Liu, H. Yu, Chemical Communications, 55 (2019) 2138-2141.

[11] J. Tu, S. Wang, S. Li, C. Wang, D. Sun, S. Jiao, Journal of The Electrochemical Society, 164 (2017) A3292-A3302.

[12] S.K. Das, Angewandte Chemie International Edition, 57 (2018) 16606-16617.

[13] G. Kresse, J. Hafner, Physical Review B, 47 (1993) 558-561.

[14] J.P. Perdew, K. Burke, M. Ernzerhof, Physical Review Letters, 77 (1996) 3865-3868.

[15] G. Kresse, J. Furthmüller, Computational Materials Science, 6 (1996) 15-50.

[16] Z. Li, J. Li, X. Li, W. Zhang, Journal of Power Sources, 467 (2020) 228323.

[17] D. Muñoz-Torrero, A. Molina, J. Palma, E. Ventosa, R. Marcilla, Carbon, 167 (2020) 475-484.

[18] H. Huang, F. Zhou, P. Lu, X. Li, P. Das, X. Feng, K. Müllen, Z.-S. Wu, Energy Storage Materials, 27 (2020) 396-404.

[19] P. Bhauriyal, A. Mahata, B. Pathak, Physical Chemistry Chemical Physics, 19 (2017) 7980-7989.

[20] Q. Bu, X. Cao, S. Li, J. Bao, Journal of Energy Storage, 52 (2022) 104994.

[21] Q. Bu, S. Zhao, X. Liu, J. Bao, Journal of Energy Storage, 50 (2022) 104254.

[22] A.C. Ferrari, J. Robertson, Physical Review B, 61 (2000) 14095-14107.

[23] F. Tuinstra, J.L. Koenig, The Journal of Chemical Physics, 53 (1970) 1126-1130.

[24] C. Thomsen, S. Reich, Physical Review Letters, 85 (2000) 5214-5217.

[25] A.C. Ferrari, J.C. Meyer, V. Scardaci, C. Casiraghi, M. Lazzeri, F. Mauri, S. Piscanec, D. Jiang, K.S. Novoselov, S. Roth, A.K. Geim, Physical Review Letters, 97 (2006) 187401.

[26] R.J. Nemanich, S.A. Solin, Physical Review B, 20 (1979) 392-401.

[27] M. Balabajew, H. Reinhardt, N. Bock, M. Duchardt, S. Kachel, N. Hampp, B. Roling, Electrochimica Acta, 211 (2016) 679-688.

[28] R.J. Nemanich, S.A. Solin, D. Gúerard, Physical Review B, 16 (1977) 2965-2972.

[29] W. Zhao, P.H. Tan, J. Liu, A.C. Ferrari, Journal of the American Chemical

Society, 133 (2011) 5941-5946.

[30] R. Thomas, S.P. Patole, P.M.F.J. Costa, Journal of Power Sources, 435 (2019) 226780.

[31] X. Dong, H. Chen, H. Lai, L. Wang, J. Wang, W. Fang, C. Gao, Journal of Energy Chemistry, 66 (2022) 38-44.

[32] C.-J. Pan, C. Yuan, G. Zhu, Q. Zhang, C.-J. Huang, M.-C. Lin, M. Angell, B.-J. Hwang, P. Kaghazchi, H. Dai, Proceedings of the National Academy of Sciences, 115 (2018) 5670-5675.

[33] J. Yu, X. Li, N. Li, T. Wu, Y. Liu, C. Li, J. Liu, L. Wang, Small Methods, 6 (2022) 2200026.

[34] K.S. Mohandas, N. Sanil, M. Noel, P. Rodriguez, Carbon, 41 (2003) 927-932.

[35] G.A. Elia, I. Hasa, G. Greco, T. Diemant, K. Marquardt, K. Hoeppner, R.J. Behm, A. Hoell, S. Passerini, R. Hahn, Journal of Materials Chemistry A, 5 (2017) 9682-9690.

[36] H. Chen, H. Xu, S. Wang, T. Huang, J. Xi, S. Cai, F. Guo, Z. Xu, W. Gao, C. Gao, Science Advances, 3 (2017) eaao7233.

[37] P.-A. Cazade, R. Hartkamp, B. Coasne, The Journal of Physical Chemistry C, 118 (2014) 5061-5072.

[38] R.M.N.M. Rathnayake, T.T. Duignan, D.J. Searles, X.S. Zhao, Physical Chemistry Chemical Physics, 23 (2021) 3063-3070.